Journal of Materials Chemistry A

Accepted Manuscript

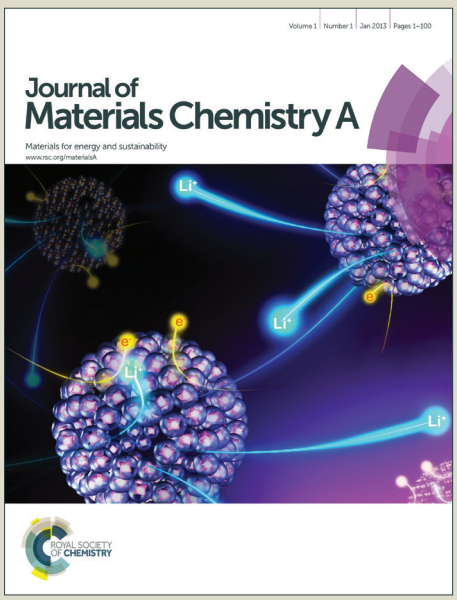

ROYAL SOCIETY OF CHEMISTRY

www.rsc.org/materialsA

Crystal Chemistry, Magnetic and Photocatalytic Properties of a New Ternary Rare-Earth Mixed Chalcogenide, $Dy_4S_4Te_3$

Sheng-Ping Guo[a,b] and Guo-Cong Guo[a,*]

[a]*State Key Laboratory of Structural Chemistry, Fujian Institute of Research on the Structure of Matter, Chinese Academy of Sciences, Fuzhou, Fujian, 350002, P. R. China.*

[b]*College of Chemistry & Chemical Engineering, Yangzhou University, Yangzhou, Jiangsu, 225002, P. R. China.*

E-mail: gcguo@fjirsm.ac.cn

Abstract The ternary dysprosium sulfur telluride, $Dy_4S_4Te_3$, was synthesized by a facile solid-state route with boron as the reducing reagent. It crystallizes in the space group *C*2/*m* of the monoclinic system with a = 6.720(1), b = 13.748(2), c = 6.715(1) Å and β = 103.36(1) º, belonging to the $Ho_4S_4Te_{2.68}$ structure type, and its 3-D structure features 2-D ladder-like $(DyS)_n$ layers linked by Dy–Te1 and Dy–Te2 bonds with additional Te1–Te1 dumbbells. The $(DyS)_n$ layers compared to the $(DyQ)_n$ (Q = S, Se and Te) layers in other binary Dy–Q compounds are discussed. The magnetic susceptibility measurement shows its paramagnetic behavior. The investigation of optical property indicates its energy gap of 1.43 eV, which is also verified by the electronic band structure calculation via Vienna *ab initio* simulation package (VASP). The photocatalytic behavior of the polycrystalline powder sample investigated by decomposing Rhodamine B under halogen lamp irradiation indicates that its photocatalytic activity can be comparable to that of Degussa P25 TiO_2.

Key words: rare earth chalcogenide, crystal structure, photocatalysis, magnetism, theory calculation

Introduction

Beyond their diverse crystal structures, metal chalcogenides are receiving much interest in view of their potential applications in the fields of thermoelectricity,[1] solar cell,[2]

second-order nonlinear optics (NLO)[3] and photocatalysis,[4] all of whom are the research hot topics all over the world in recent years. It is well known that one material's physical behaviors are dependent on its own structure, which means that it can be predicted reasonably that whether one material has the desired property performance based on its structure information. Metal chalcogenides are often semiconductors with the energy gap between 0 and 3 eV, which can be easily obtained via either ultraviolet-invisible-near infrared spectrum characterization or electronic band structure theory calculation. Interestingly, all the above mentioned application fields for metal chalcogenides have demands on the materials' energy gaps. For photocatalytic active crystalline semiconductors, their optical absorptions follow the equation, $\alpha = A\ (h\nu - Eg)^{n/2}/h\nu$,[5] where α, A, ν, Eg and n denote absorption coefficient, incident light frequency, constant, band gap, and an integer, respectively. As thermoelectric materials, their TE ability can be expressed as $ZT = (S^2\sigma/\kappa)T$, where ZT, S, σ, κ and T mean the thermoelectric figure of merit, thermopower, electrical conductivity, thermal conductivity and temperature, respectively. For chalcogenides used in solar cell, to control their band gaps is important in terms of tailoring the properties of the absorber layer to match the incident solar radiation spectrum and to optimize the device efficiency.[6] In case of second-order NLO materials, their laser induced damage threshold will be enhanced if their energy gap can be increased. Go so far as to chalcogenides-based photocatalyst, charge carriers (electron and hole) can be generated and used to catalyze the chemical reaction when they are exposed to light energies comparable to their band gaps.[7] Based on these theoretical considerations, metal chalcogenides' multi-physical performances can be improved once their energy gaps are appropriately tuned.

In recent years, there are many metal chalcogenides being explored as ultraviolet or visible light-driven photocatalyst since they have suitable energy gaps, these include, but not limit to CdS,[8] $B^{II}In_2S_4$ (B^{II} = Zn, Cd),[9] $AgGaS_2$-type,[10] ZnS-$CuInS_2$-$AgInS_2$ solid solution,[11] A^I_2-B^{II}-Q^{IV}-S_4 (A^I = Cu and Ag; B^{II} = divalent transition metal; Q^{IV} = Sn and Ge),[12] $(AgIn)_xZn_{2(1-x)}S_2$ solid solution,[13] $AGa_2In_3S_8$ (A = Cu, Ag),[14] La_2CdS_4[15] and open framework chalcogenides.[16] The photocatalytic splitting of water into hydrogen and oxygen and the

photocatalytic degradation of organic pollutants are promising technologies to solve the urgent energy and environmental issues in the world, so continuous to look for new photocatalysts and improve the known photocatalysts' performances are interesting and challengeable work for both chemists and material scientists.

Combining the social demand and our group's rich experiences in synthesizing metal chalcogenides,[17] we started to explore new chalcogenide-type photocatalyst recently. In the present work, $Dy_4S_4Te_3$, a new ternary rare-earth mixed chalcogenide, was obtained by high-temperature solid-state reaction. Its 3-D structure features 2-D ladder-like $(DyS)_n$ layer and Te–Te dumbbell. Herein, we report its synthesis, crystal structure, optical, magnetic and photocatalytic properties, together with electronic band structure calculation complemented by VASP software. Interestingly, $Dy_4S_4Te_3$ exhibits photocatalytic activity under halogen lamp irradiation which can be comparable to that of Degussa P25 TiO_2.

Experimental Section

Synthesis and analyses. All starting materials were used as received without further purification. Single crystals of the title compound were obtained by solid-state reaction with KI as flux. The starting materials are Dy_2O_3 (99.9%), S (99.999%), Te (99.999%) and additional boron powder (99%). The sample has a total mass of 500 mg and 400 mg KI (99%) additional, and the molar ratios of elements Dy : S : Te : B are 4 : 4 : 3 : 6. The mixture of starting materials was ground into fine powders in an agate mortar and pressed into a pellet, followed by being loaded into a quartz tube. The tube was evacuated to be 1×10^{-4} torr and flame-sealed. The sample was placed into a muffle furnace, heated from the room temperature to 573 K in 5 h and equilibrated for 10 h, followed by heating to 923 K in 5 h and equilibrated for 10 h, then heated to 1223 K in 5 h and homogenized for 10 days, finally cooled down to 573 K in 5 days and powered off. The black prismatic crystals of $Dy_4S_4Te_3$ stable in moisture and air were obtained and hand-picked under a microscope, then washed using ethanol and water under ultrasonic wave, whose purity was confirmed by powder X-ray diffraction (PXRD) study. The PXRD pattern was collected with a Rigaku DMAX 2500 diffractometer at 40 kV and 100 mA for Cu-$K\alpha$ radiation (λ = 1.5406 Å) with a scan speed of 5 °/min at room

temperature. The simulated pattern was produced using the Mercury v1.4 program provided by the Cambridge Crystallographic Data Center and single-crystal reflection data. The PXRD pattern of $Dy_4S_4Te_3$ (Figure S1) corresponds well with the simulated one, indicating of almost single phase of the selected crystals. Semiquantitative microscope element analysis on several single crystals of $Dy_4S_4Te_3$ was performed on a field-emission scanning electron microscope (FESEM, JSM6700F) equipped with an energy dispersive X-ray spectroscope (EDS, Oxford INCA), which confirmed the presence of Dy, S and Te with the approximate composition of $Dy_{1.3}S_{1.2}Te$, and no other elements were detected. The exact composition was established from the X-ray structure determination.

Structure determination. The intensity data set was collected on Rigaku AFC7R X-ray diffractometers with graphite-monochromated Mo-$K\alpha$ radiation (λ = 0.71073 Å) using ω-2θ scan technique and reduced by CrystalStructure software.[18] The structure of $Dy_4S_4Te_3$ was solved by direct method and refined by full-matrix least-squares techniques on F^2 with anisotropic thermal parameters for all atoms. All the calculations were performed with Siemens SHELXTL^{TM} version 5 package of crystallographic software.[19] The final refinement included anisotropic displacement parameters for all atoms and a secondary extinction correction. The crystallographic data and selected bond lengths are listed in Tables 1-2. CIF has also been deposited with Fachinformationszentrum Karlsruhe, 76344 Eggenstein-Leopoldshafen, Germany [fax: (49) 7247-808-666; e-mail: crysdata@fiz.karlsruhe.de] with depository number CSD-428130.

The crystal structure of $Dy_4S_4Te_3$ was refined to be centrosymmetric monoclinic space group $C2/m$, and the composition derived from the structure solution is comparable to the result of energy dispersive X-ray spectroscope (EDS) analysis. It must be pointed out here that the two strongest Fourier peaks around Te1 and Te2, respectively, should be considered as the residual peaks though they have high U_{eq} values because the distances between them and their nearest Te atoms are 1.44 (Q1–Te2) and 1.40 (Q2–Te1) Å, respectively. We have synthesized and collected the intensity data set of $Dy_4S_4Te_3$ repeatedly for more than ten times using different crystals, however, such two peaks with the similar large U_{eq} and same

atomic coordinates always appeared.

Table 1. Crystal data and structure refinement parameter of $Dy_4S_4Te_3$.

chemical formula	$Dy_4S_4Te_3$
Fw	1161.04
crystal Size (mm^3)	0.10 × 0.06 × 0.04
T (K)	293(2)
λ (Mo Kα, Å)	0.71073
crystal system	Monoclinic
space group	$C2/m$
a (Å)	6.720(1)
b (Å)	13.748(2)
c (Å)	6.715(1)
β (°)	103.36(1)
V ($Å^3$)	603.6(2)
Z	2
D_{calcd} (g cm^{-3})	6.388
μ (mm^{-1})	32.210
F(000)	968
θ range (°)	2.96 to 25.47
indep. reflns/R_{int}	582/0.0563
obs. reflns	639
$R1$[a] ($I > 2\sigma(I)$)	0.0481
wR2[b] (all data)	0.1186
GOF on F^2	0.996

[a] $R1 = ||F_o| - |F_c||/|F_o|$. [b] $wR2 = [w(F_o^2 - F_c^2)^2]/[w(F_o^2)^2]^{1/2}$.

Table 2. Selected bond distances (Å) of $Dy_4S_4Te_3$.[a]

Bond	Dist.	Bond	Dist.
Dy(1)-S(1)	2.682(4)	Dy(1)-Te(2)	3.074(1)
Dy(1)-S(2)	2.726(2)	Dy(1)-Te(1)#3	3.296(1)
Dy(1)-S(2)#1	2.729(3)	Dy(1)-Te(1)	3.317(1)
Dy(1)-S(1)#2	2.746(2)	Te(1)-Te(1)#3	2.796(3)

[a]Symmetry codes: #1 -x+1/2, -y+1/2, -z+1; #2 -x+1/2, -y+1/2, -z; #3 -x, -y+1, -z.

Physical measurements. The variable-temperature magnetic susceptibility on polycrystalline powder of $Dy_4S_4Te_3$ ground and loaded into gelatin capsules was measured with a Quantum Design PPMS model 6000 magnetometer in the temperature range of 2–300 K at a constant field of 5000 Oe. The diamagnetic corrections for all data were made using Pascal's constants.[20]

The diffuse reflectance spectrum was recorded at the room temperature on a computer-controlled Lambda 900 UV–Vis–NIR spectrometer equipped with an integrating sphere in the wavelength range of 300–1700 nm. A $BaSO_4$ plate was used as a reference, on which the finely ground powdery sample was coated. The absorption spectrum was calculated from reflection spectrum by the Kubelka-Munk function.[21]

The sample used to test photocatalytic behavior of $Dy_4S_4Te_3$ was obtained using agate mortar to grind the prismatic crystals to several micrometer powders, which was characterized by SEM (FESEM, JSM6700F) technique (Figure S4). Photocatalytic activity of $Dy_4S_4Te_3$ was monitored by decomposing Rhodamine B (RhB) at room temperature.[22] 30 mg of $Dy_4S_4Te_3$ was dispersed in 100 mL RhB aqueous solution (5×10^{-6} mol/L) in a tubular glass container with an inner diameter of 4.0 cm. After being stirred without irradiation for 60 min, the adsorption/desorption of RhB molecules on powder of $Dy_4S_4Te_3$ reached equilibrium. The mixture was further stirred in front of a 500-W halogen lamp and cooled by quickly running air to avoid additional heating effects. The distance between light source and glass container was 20 cm. The concentration of RhB was tested by UV/Vis absorption spectra on a Perkin-Elmer Lambda 35 UV/Vis spectrophotometer. Under the same experimental conditions, the photocatalytic activity of commercial photocatalyst Degussa P25 TiO_2 was also measured to estimate the photocatalytic activity of $Dy_4S_4Te_3$.

Calculation details. The calculation model was built directly from the single-crystal diffraction data of $Dy_4S_4Te_3$. The electronic structure calculation including band structure and density of states based on density functional theory (DFT) was performed using VASP. The generalized gradient approximation (GGA) was chosen as the exchange-correlation functional and a plane wave basis with the projector-augmented wave (PAW) potentials was used. The

plane-wave cutoff energy of 280 eV and the threshold of 10^{-5} eV were set for the self-consistent-field convergence of the total electronic energy. The electronic configurations for Dy, S and Te atoms were 5d and 4f, 3s and 3p, 5s and 5p, respectively. The numerical integration of the Brillouin zone was performed using 4 × 4 × 4 Monkhorst–Pack *k*-point meshes for $Dy_4S_4Te_3$ and the Fermi level (E_f = 0 eV) was selected as the reference.

Results and discussion

Crystal structures. $Dy_4S_4Te_3$ crystallizes in the monoclinic space group *C*2/*m*, belonging to the $Ho_4S_4Te_{2.68}$ structure type (Pearson symbol *mS*22).[23] A similar compound $Dy_4S_4Te_{2.3}$ has been reported in 1976,[24] where the occupancies of Te1 and Te2 atoms were refined to be 0.88 and 0.56, respectively. Initially, we thought our compound might be $Dy_4S_4Te_{2.3}$ when we tried to resolve the crystal structure of $Dy_4S_4Te_3$, however, the occupancies of both Te1 and Te2 in $Dy_4S_4Te_3$ were very close to 1 when freely refining their occupancies even if their temperature factors are relatively high, indicating that there is no disorder in the crystal structure. On the other hand, the cell parameters of $Dy_4S_4Te_3$ (a = 6.720 (1) Å, b = 13.748(2) Å, c = 6.715(1) Å and β = 103.36(1) º) are larger than those of $Dy_4S_4Te_{2.3}$ (a = 6.67 Å, b = 13.72 Å, c = 6.67 Å and β = 102.83 º). Based on these considerations, $Dy_4S_4Te_3$ is indeed a new compound without disorder, unlike disorders discovered in $Ho_4S_4Te_{2.68}$ and $Dy_4S_4Te_{2.3}$. The different compositions of the isostructural $Dy_4S_4Te_3$ and $Dy_4S_4Te_{2.3}$ may be influenced by the synthetic methods. The latter was obtained from the reactions of Dy_2S_3, Dy_2Te_3 and Te, while the title compound was synthesized through the reactions of Dy_2O_3, S, Te, and B with KI as flux.

There are one Dy, two S (S1 and S2) and two Te (Te1 and Te2) atoms in the crystallographically independent unit in the structure of $Dy_4S_4Te_3$. Each Dy atom is seven-coordinated with two S1, two S2, two Te1 and one Te2 atoms to form DyQ_7 (Q = S, Te) coordination geometry (Figure S2). The 3-D crystal structure of $Dy_4S_4Te_3$ features 2-D ladder-like $(DyS)_n$ layers connected with each other via Te atoms (Figure 1). If not considering Te atoms, each Dy atom has four neighboring S atoms and situates at the top of the tetragonal pyramid DyS_4. As can be seen in Figure 2a, the two types of S atoms are

arranged alternatively and no interactions between them. Taking tetragonal pyramid DyS_4 as a whole marked "*A*", each *A* is connected with other eight A on the 2-D ladder-like layer when viewing along the *b* direction. *A* shares S edge with four A having the Dy–Dy distances of 4.131 (1), 4.164 (1) × 2, 4.196 (1) Å, respectively, and shares S corner with the other four A with the Dy–Dy distances of 4.051 (1), 4.279 (1), 5.233 (1) and 5.310 (1) Å, respectively (Figure 2a and 2c). Interestingly, the centered Dy^{3+} ion together with other four Dy^{3+} ions, which are connected by sharing S edges, are located on one plane parallel to the *ac* plane, and the other four Dy^{3+} ions connected with the centered Dy^{3+} ion by sharing S atoms are also located on one plane, which is parallel to the *ac* plane, too (Figure 2c). The distance between these two parallel planes is 2.46 Å. The $(DyS)_n$ layers are connected through Te1 and Te2 atoms, and the linkage between Dy and Te atoms is drawn in Figure 2b. It can be seen that each Dy^{3+} ion (denoted as *B*) has five nearest Dy^{3+} ions (denoted as *C*) featuring the six Dy^{3+} ions located in the *ab* plane, and *B* and *C* are connected via sharing corner (Te2), edge (Te1–Te1 dumbbell) or face (Te1–Te1 dumbbell and Te2), respectively.

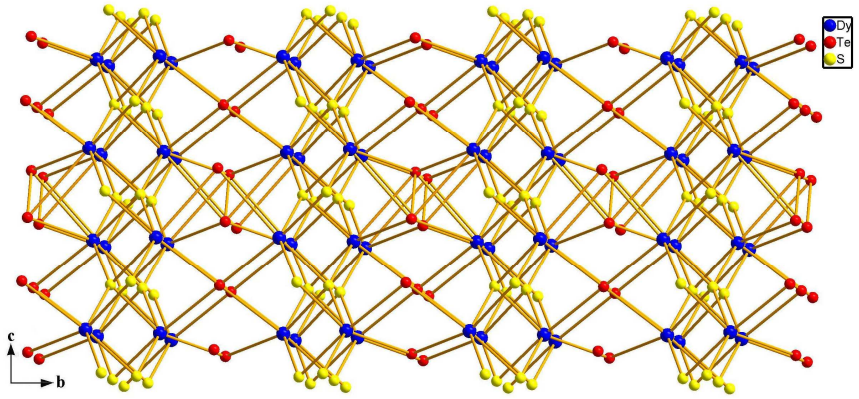

Figure 1. A ball-and-stick representation of the 3-D structure of $Dy_4S_4Te_3$ viewed along the *a* direction. Dy, S and Te atoms are represented as blue, yellow and red spheres, respectively.

The Dy–S bond distances in $Dy_4S_4Te_3$ are in the range of 2.682(4)–2.746(2) Å, which is close to the Dy–S bond lengths in $Al_{0.50}Dy_3(Si_{0.50}Al_{0.50})S_7$ and $Al_{0.38}Dy_3(Si_{0.85}Al_{0.15})S_7$.[17b] The Dy–Te bond distances of 3.074(1)–3.317(1) Å is similar with 3.029(2)–3.290(5) Å discovered in Dy_2Te.[25] The Te–Te dumbbells with the distance of 2.796(3) Å is comparable to 2.7895(6) Å happened in $BaCu_{5.7}Se_{0.5}Te_{6.5}$[26] and 2.776(1) Å in $KPrTe_4$.[27]

When we account for the oxidation states of the atoms in $Dy_4S_4Te_3$, the Dy, S and Te2

atoms' oxidation states can be readily assigned as +3, –2 and –2, respectively, while for Te1 atom, its oxidation state should be –1 because of its dimeric character.

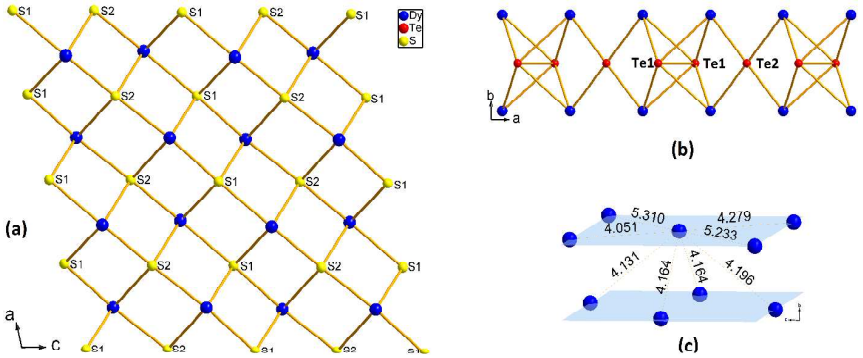

Figure 2. (a) 2-D ladder-like $(DyS)_n$ layer in $Dy_4S_4Te_3$ constructed by Dy–S bonds viewing along the *b* direction; (b) 1-D chain constructed by Dy–Te bonds along the *a* direction; (c) Dy–Dy distances. Each Dy^{3+} ion has eight surrounding Dy^{3+} ions, four located in one plane with the centered Dy^{3+} ion, and the other four in another plane parallel to the aforementioned plane. Dy, S and Te atoms are depicted as blue, yellow and red spheres, respectively.

In order to investigate the structural relationship between $Dy_4S_4Te_3$ and known binary or ternary dysprosium chalcogenides, their crystal structures were checked based on their cif documents downloaded from the ICSD database or Pearson's database. There are many binary Dy–Q compounds reported in the past years, which have rich compositions and various crystal structures. Relatively, very few ternary Dy–Q'–Q'' mix-chalcogenides were discovered. The $(DyQ)_n$ layers composed of Dy and Q atoms arranged alternatively can also be isolated in the structures of several binary chalcogenides summarized in Table 3. Totally, there are four different types of such layers discovered in eight binary Dy–Q compounds, namely, DyS (*Fm*-3*m*), DyS_2 (*P*4/*nmmz*), DyS_2 (*P*-4*b*2), $DySe_{1.84}$ (*Pmn*2$_1$), $Dy_8Se_{14.8}$ (*Amm*2), $DyTe_3$ (*Cmcm*), Dy_2Te_3 (*Fddd*) and Dy_2Te_5 (*Cmcm*). The various $(DyQ)_n$ slabs are evidently different from the case in $Dy_4S_4Te_3$ as shown in Figure 3.

Table 3. Crystal Structures of known binary Dy–Q compounds (Q = S, Se and Te).[a,b]

Compound	Space Group	Pearson Symbol	Structure Type	2-D $(DyQ)_n$ layer
DyS	*Fm*-3*m*	*cF*8	NaCl	multi-
DyS_2	*P*4/*nmmz*	*tP*6	UAs_2	single

DyS_2	*P*-4*b*2	*tP*24	NdS_2	double
DyS_2	*Fd*-3*ms*	-	-	no
Dy_2S_3	*Pnma*	*oP*20	Cr_3S_2	no
Dy_2S_3	$P2_1/m$	*mP*30	Ho_2S_3	no
Dy_3S_4	*I*-43*d*	*cI*128	Th_3P_4	no
Dy_5S_7	*C*2/*m*	*mS*24	Y_5S_7	no
DySe	$P6_3mc$	*hP*4	ZnO	no
$DySe_{1.84}$	$Pmn2_1$	*oP*6	$DySe_{1.84}$	double
Dy8Se14.8	*Amm*2	*tP*6	superstructure of ZrSiS	double
Dy_2Te	*Pnma*	*oP*36	Sc_2Te	no
$DyTe_3$	*Cmcm*	*oS*16	$ErTe_3$	double
Dy_2Te_3	*Fddd*	*oF*80	Sc_2S_3	single
Dy_2Te_5	*Cmcm*	*oS*28	Nd_2Te_5	double

[a]All the data based on their cif files downloaded from the ICSD database or Pearson's crystal database.

[b]Only one of them summarized here if two Dy–Q compounds crystallize in the same structures.

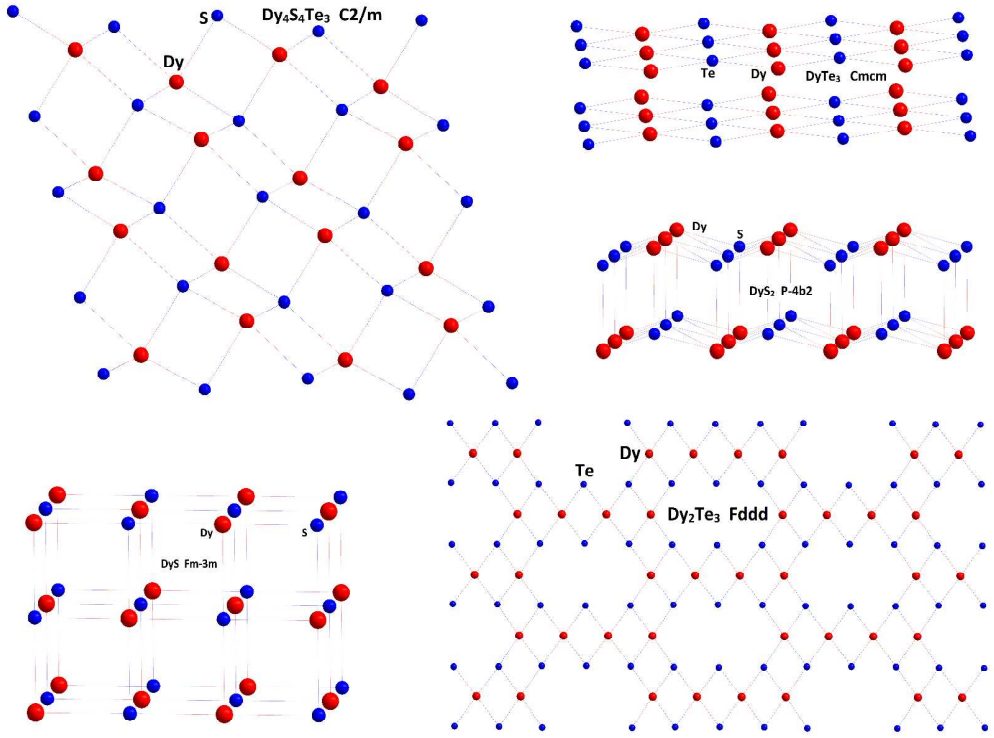

Figure 3. The comparisons of $(DyS)_n$ layers in the crystal structures of $Dy_4S_4Te_3$ and other binary Dy–Q compounds. Only four types of $(DyS)_n$ layers can be found in binary Dy–Q compounds' structures, which shown here include DyS (*Fm*-3*m*), DyS_2 (*P*-4*b*2), $DyTe_3$ (*Cmcm*) and Dy_2Te_3 (*Fddd*). Dy and Q atoms are

depicted as red and blue spheres, respectively, and the Dy–Q bonds are drawn as thin two-colored sticks.

The puckered $(DyQ)_n$ double layers linked by Dy–Q bonds appear in the crystal structures of DyS_2 (*P*4/*nmmz*), DyS_2 (*P*-4*b*2), $DySe_{1.84}$ (*Pmn*2$_1$), $Dy_8Se_{14.8}$ (*Amm*2) and Dy_2Te_5 (*Cmcm*). Different from the linked double layers, isolated puckered $(DyTe)_n$ double layers happen in the rich-Te compound $DyTe_3$ (*Cmcm*), while it has to be mentioned that the single layers in these six Dy–Q compounds are totally same. The $(DyQ)_n$ layers found in Dy_2Te_3 (*Fddd*) is not puckered, but planar, which is special as it forms cavities surrounded by six Dy and six Te atoms. Each Dy atom is coordinated with four nearest Te atoms, but there are two types of coordination geometries for Te atoms, one type is that one Te atom is just surrounded by two Dy atoms forming V-shape unit, and the other one is $TeDy_3$ unit seeming like λ-shape. Finally, there is a planar $(DyQ)_n$ multi-layer linked by Dy–S bonds can be found in DyS (*Fm*-3*m*).

Besides the crystal structure analysis, the further investigation on $Dy_4S_4Te_3$'s physical properties was also performed in this study, which is first for the $RE_4S_4Te_{3-x}$ family members though $Ho_4S_4Te_{2.68}$ and $Dy_4S_4Te_{2.3}$ were reported many years ago.

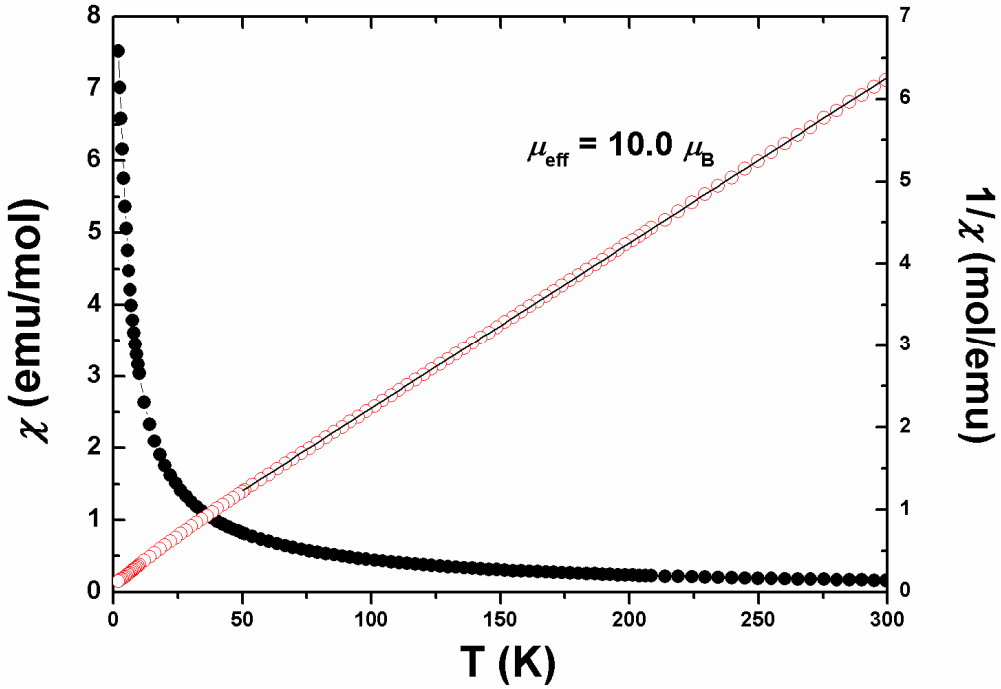

Figure 4. Temperature dependence of the magnetic susceptibility and inverse susceptibility of $Dy_4S_4Te_3$. Inverse susceptibility vs temperature was linearly fit to the Curie-Weiss law.

Magnetism. Temperature dependent DC magnetization measurement was performed on

polycrystalline sample of $Dy_4S_4Te_3$ within the range from 2–300 K under an applied field of 5000 Oe. The data was converted to molar magnetic susceptibility (χ_m = M/H), and the χ_m (T) and $1/\chi_m$ (T) plots are shown in Figure 4. In the high temperature regime, the sample is paramagnetic as expected for systems with core 4*f*-electrons. The data for $Dy_4S_4Te_3$ follows the Curie-Weiss law $\chi(T) = C/(T-\theta_p)$,[28] where C is the Curie constant and θ_p is the paramagnetic Weiss temperature. Curie constants and effective magnetic moment of $Dy_4S_4Te_3$ can be deduced from the linear fit of the inverse magnetic susceptibility vs. temperature. The obtained moment is 10.0 μ_B, much close to the theory value expected for free-ion Dy^{3+} according to the Hund's rule.[28] Down to the lowest temperature (2 K), no apparent signal of magnetic order can be detected.

Theory investigation. To investigate the electronic structure of $Dy_4S_4Te_3$, the band structure together with densities of states (DOS) computations based on the DFT theory were performed using VASP software. The calculated band structure along high symmetry points of the first Brillouin zone is shown in Figure 5, from which it can be seen that the lowest conduction band (CB) is located at V point, while the highest valence band (VB) located at A point, indicating that $Dy_4S_4Te_3$ is an indirect band gap semiconductor with the band gap of 1.42 eV, which is very close to the experimental 1.43 eV obtained via diffuse reflection spectrum measured at room temperature (Figure S3). The energy gap of 1.43 eV is in accordance with its black color.

The total and partial densities of states (DOS and PDOS) of $Dy_4S_4Te_3$ are plotted in Fig. 9. The highest VB is constituted of Te-5p, S-3p and Dy-5d, together with minor Te-5s. The lowest CB is composed of Te-5p, Dy-5d and weak S-3p. The valence bands (VB) between –4.4 and –0.4 eV are originated mainly from S-3s, Te-5p and Dy-5d orbitals, and additional minor Dy-6p. The conduction bands ranging from 2.5 to 4.0 eV are primarily consisted of Dy-5d together with minor S-3p and Te-5p orbitals. Briefly, the energy gap of $Dy_4S_4Te_3$ is determined by the S-3p, Te-5p and Dy-5d orbitals, the respective valence orbitals of S^{2-}, Te^{2-}, Te^{1-} and Dy^{3+} ions.

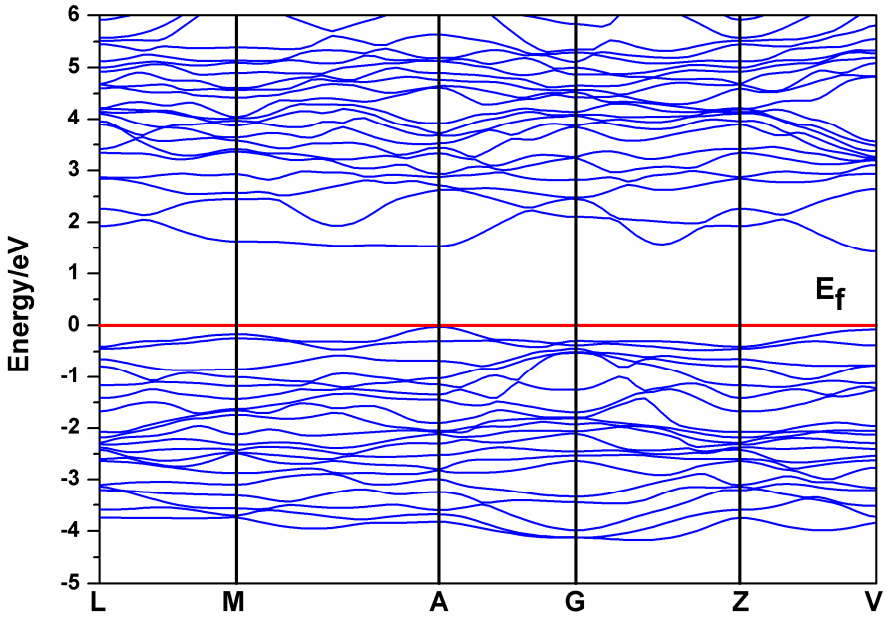

Figure 5. Calculated band structure of $Dy_4S_4Te_3$. The Fermi level is chosen as the energy reference at 0 eV and the band gap is calculated to be 1.42 eV.

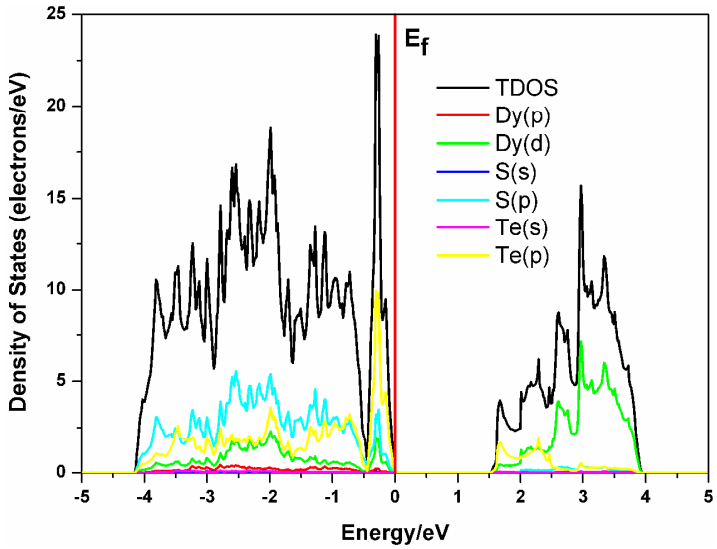

Figure 6. Calculated total and partial density of states (TDOS and PDOS) for $Dy_4S_4Te_3$. The Fermi level is chosen as the energy reference at 0 eV.

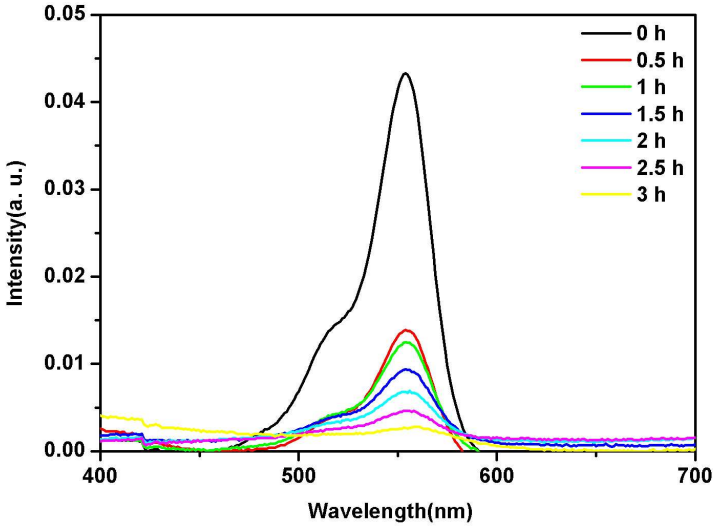

Figure 7. Absorption spectra of RhB aqueous solutions at different intervals in the presence of polycrystalline powder of $Dy_4S_4Te_3$. The characteristic absorption peak of RhB is located at 553 nm.

Photocatalytic Activity. It is well-known that a photocatalyst absorbs ultraviolet or visible light irradiation from an illuminated light source or sunlight. The Gibbs free energy for water splitting into H_2 and O_2 is 237 kJ/mol, which is amount to 1.23 eV, therefore, the band gap energy of photocatalyst driving H_2O decomposed should be more than 1.23 eV.[29] Indeed, the preferable band gap is around 2 eV for photocatalyst to utilize the maximum portion of the visible light,[30] and that is the reason why there are so many studies about chalcogenides explored as visible light driving photocatalyst in recent years. In view of these considerations, the photocatalytic behaviors of $Dy_4S_4Te_3$ are only investigated under ultraviolet light, through degradation of organic dye RhB and decomposition of H_2O.

Comparative experiments were carried out to investigate the potential photocatalyitc behaviors of polycrystalline powder of the as-prepared $Dy_4S_4Te_3$ in the photo-degradation of organic contaminant RhB under ultraviolet light irradiation. The results are shown in Figures 7 and 8. It can be viewed that the characteristic absorption peak of RhB at 553 nm was used as a monitored parameter during the photocatalytic degradation process. Figure 7 shows the absorption spectra of aqueous solutions of RhB measured at different intervals in the presence of $Dy_4S_4Te_3$. About 90% of RhB was degraded after 3 hours halogen lamp irradiation. For comparison, the photocatalytic degradation of RhB was carried out in the presence of Degussa P25 TiO_2 and absence of photocatalyst under halogen lamp irradiation (Figure 8). It can be

observed that the photocatalytic activity of $Dy_4S_4Te_3$ is comparable to that of Degussa P25 TiO_2, while there is very small degradation of RhB without any photocatalyst. The degradation process can be simply expressed as follows. After absorption energy from halogen lamp irradiation, photo-electron and hole will be produced in view of $Dy_4S_4Te_3$'s energy gap of 1.43 eV. These photo-electrons will be captured by the soluble O_2 on the surface of $Dy_4S_4Te_3$ particles to form superoxide anions, while the holes will oxidate OH^- and water on the surface of $Dy_4S_4Te_3$ to hydroxyl radicals. These superoxide anions and hydroxyl radicals finally degrade RhB to carbon dioxide and water because of their strong oxidizability. Though the result is not very encouraging, it can be supposed that nano-sized $Dy_4S_4Te_3$ should have better photocatalytic performances to degrade organic contaminants.

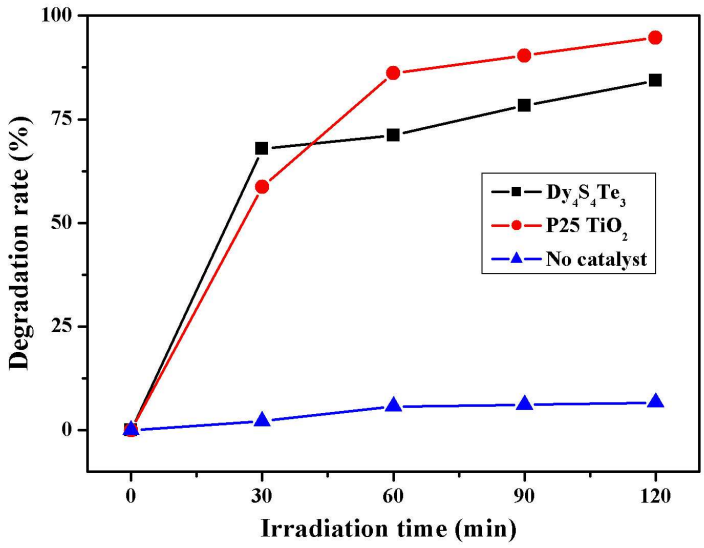

Figure 8. Degradation rates of RhB at different intervals in the presence of polycrystalline powder of $Dy_4S_4Te_3$ (black) or Degussa P25 TiO_2 (red), and absence of photocatalyst (blue).

The polycrystalline powder of the as-prepared $Dy_4S_4Te_3$ was also tested to decompose water, however, no obvious photocatalytic behavior could be observed in the present of $Dy_4S_4Te_3$.

Conclusions.

A new chalcogenide photocatalyst has been synthesized by solid-state reaction, and its crystal structure features 2-D ladder-like $(DyS)_n$ layers and Te–Te bonds. Its physical

properties were investigated, including magnetic, optical and photocatalytic properties. The results indicate paramagnetic behavior and photocatalytic activity to degrade organic contaminant RhB under ultraviolet light irradiation. Its optical properties were also checked by combining ultraviolet-visible spectrum and theory calculations, and the results demonstrate that it is an indirect energy gap semiconductor with E_g = 1.43 eV. Totally, this study demonstrate a new interesting rare-earth mixed chalcogenide photocatalyst, and further experiments will performed on some simple rare-earth chalcogenides with similar compositions, or moving their potential application to visible light driving photocatalysis by tuning their band gaps to idea values.

Acknowledgments.

We gratefully acknowledge the financial support by the NSF of China (21221001, 91222204, 21403231), 973 program (2011CBA00505), Key Project from the CAS (KJCX2-EW-H03), and the NSF of Fujian Province (2014J05025).

Supporting information available.

Crystallographic file in CIF format and additional figures. This material is available free of charge via the Internet at xxx.

Reference

1 (a) D.-Y. Chung, T. Hogan, P. Brazis, M. Rocci-Lane, C. Kannewurf, M. Bastea, C. Uher and M. G. Kanatzidis, *Science*, 2000, **287**, 1024–1027; (b) J.-S. Rhyee, K. H. Lee, S. M. Lee, E. Cho, S. I. Kim, E. Lee, Y. S. Kwon, J. H. Shim and G. Kotliar, *Nature*, 2009, **459**, 965–968; (c) M.-L. Liu, I-W. Chen, F.-Q. Huang and L.-D. Chen, *Adv. Mater.*, 2009, **21**, 3808–3812; (d) Z.-S. Lin, L. Chen, L.-M. Wang, J.-T. Zhao and L.-M. Wu, *Adv. Mater.*, 2013, **25**, 4800–4806.

2 (a) Q. J. Guo, G. M. Ford, W.-C. Yang, B. C. Walker, E. A. Stach, H. W. Hillhouse and R. Agrawal, *J. Am. Chem. Soc.*, 2010, **132**, 17384–17386; (b) Q. J. Guo, H. W. Hillhouse and R. Agrawal, *J. Am. Chem. Soc.*, 2009, **131**, 11672–11673.

3 (a) I. Chung and M. G. Kanatzidis, *Chem. Mater.*, 2014, **26**, 849-869; (b) H. Lin, L. Chen, L.-J. Zhou and L.-M. Wu, *J. Am. Chem. Soc.*, 2013, **135**, 12914–12921; (c) X.-M. Jiang, S.-P. Guo, H.-Y. Zeng, M.-J. Zhang and G.-C. Guo, *Struct. Bonding*, 2012, **145**, 1–43.

4 (a) S. Y. Chen, A. Walsh, X.-G. Gong and S.-H. Wei, *Adv. Mater.*, 2013, **25**, 1522–1539; (b) I. Tsuji,

Y. Shimodaira, H. Kato, H. Kobayashi and A. Kudo, *Chem. Mater.*, 2010, **22**, 1402–1409; (c) B. B. Kale, J.-O. Baeg, S. M. Lee, H. Chang, S.-J. Moon and C. W. Lee, *Adv. Funct. Mater.*, 2006, **16**, 1349–1354; (d) T. Bian, L. Shang, H. J. Yu, M. T. Perez, L.-Z. Wu, C.-H. Tung, Z.-H. Nie, Z.-Y. Tang and T. R. Zhang, *Adv. Mater.*, 2014, **26**, 5613–5618; (e) H. Tong, S. X. Ouyang, Y. P. Bi, N. Umezawa, M. Oshikiri and J. H. Ye, *Adv. Mater.*, 2012, **24**, 229–251.

5 D. Wang, K. B. Tang, Z. H. Liang and H. G. Zheng, *J. Solid State Chem.*, 2010, **183**, 361–366.

6 S. Bag, O. Gunawan, T. Gokmen, Y. Zhu, T. K. Todorov and D. B. Mitzi, *Energy Environ. Sci.*, 2012, **5**, 7060–7065.

7 S. Rawalekar and T. Mokari, *Adv. Energy Mater.*, 2013, **3**, 12–27.

8 J. Jin, J. G. Yu, G. Liu and P. K. Wong, *J. Mater. Chem. A*, 2013, **1**, 10927–10934.

9 (a) L. Shang, C. Zhou, T. Bian, H. J. Yu, L.-Z. Wu, C.-H. Tung and T. R. Zhang, *J. Mater. Chem. A*, 2013, **1**, 4552–4558; (b) B. B. Kale, J.-O. Baeg, S. M. Lee, H. Chang, S.-J. Moon and C. W. Lee, *Adv. Funct. Mater.*, 2006, **16**, 1349–1354; (c) S. K. Apte, S. N. Garaje, R. D. Bolade, J. D. Ambekar, M. V. Kulkarni, S. D. Naik, S. W. Gosavi, J. O. Baeg and B. B. Kale, *J. Mater. Chem.*, 2010, **20**, 6095–6102.

10 J. S. Jang, S. H. Choi, N. Shin, C. J. Yu and J. S. Lee, *J. Solid State Chem.*, 2007, **180**, 1110–1118.

11 (a) I. Tsuji, H. Kato and A. Kudo, *Chem. Mater.*, 2006, **18**, 1969–1975; (b) I. Tsuji, H. Kato and A. Kudo, *Angew. Chem. Int. Ed.*, 2005, **44**, 3565–3568.

12 L. H. Ai and J. Jiang, *J. Mater. Chem.*, 2012, **22**, 20586–20592.

13 I. Tsuji, H. Kato, H. Kobayashi and A. Kudo, *J. Am. Chem. Soc.*, 2004, **126**, 13406–13413.

14 H. Kaga, K. Saito and A. Kudo, *Chem. Commun.*, 2010, **46**, 3779–3781.

15 B. B. Kale, J.-O. Baeg, K.-J. Kong, S.-J. Moon, L. K. Nikam and K. R. Patil, *J. Mater. Chem.*, 2011, **21**, 2624–2631.

16 (a) Z. Y. Zhang, J. Zhang, T. Wu, X. H. Bu and P. Y. Feng, *J. Am. Chem. Soc.*, 2008, **130**, 15238–15239; (b) N. F. Zheng, X. H. Bu, H. Vu and P. Y. Feng, *Angew. Chem. Int. Ed.*, 2005, **44**, 5299 –5303.

17 (a) S.-P. Guo, G.-E. Wang, M.-J. Zhang, M.-F. Wu, G.-N. Liu, X.-M. Jiang, G.-C. Guo and J.-S. Huang. *Dalton Trans.* 2013, **42**, 2679–2682; (b) S.-P. Guo, G.-C. Guo, M.-S. Wang, J.-P. Zou, G. Xu, G.-J. Wang, X.-F. Long, J.-S. Huang, *Inorg. Chem.*, 2009, **48**, 7059–7065; (c) S.-P. Guo, G.-C. Guo, M.-S. Wang, J.-P. Zou, H.-Y. Zeng, L.-Z. Cai, J.-S. Huang, *Chem. Commun.*, 2009, **29**, 4366–4368; (d) M.-J. Zhang, X.-M. Jiang, L.-J. Zhou and G.-C. Guo, *J. Mater. Chem. C*, 2013, **1**, 4754–4760; (e) S.-H. Lin, J.-G. Mao, G.-C. Guo and J.-S. Huang. J. Alloy & Compd., 1997, 252, L8-L11.

18 Rigaku, *CrystalStructure Version 3.6.0*, Rigaku Corporation, 2002.

19 Siemens, *SHELXTL™ Version 5 Reference Manual*, Siemens Energy & Automation Inc., Madison, Wisconsin, USA, 1994.

20 E. A. Boudreaux and J. N. Mulay, Eds. *Theory and Application of Molecular Paramagnetism*, J. Wiley and Sons, New York, 1976.

21 (a) W. W. Wendlandt and H. G. Hecht, *Reflectance Spectroscopy*, Interscience Publishers, New York, 1966; (b) G. Kortüm. *Reflectance Spectroscopy*, Springer, 1969.

22 T.-Y. Ding, M.-S. Wang, S.-P. Guo, G.-C. Guo and J.-S. Huang, *Mater. Lett.*, 2008, **62**, 4529–4531.

23 G. Ghémard, J. Etienne, G. Schiffmacher and J. Flahaut, *J. Solid State Chem.*, 1982, **45**, 146–153.

24 G. Ghémard, *Bull. Soc. Chim. Fr.*, 1976, 1007–1012.

25 P. S. Herle and J. D. Corbett, *Inorg. Chem.*, 2001, **40**, 1858–1864.

26 O. Mayasree, C. R. Sankar, Y. J. Cui, A. Assoud and H. Kleinke, *Eur. J. Inorg. Chem.*, 2011, 4037–4042.

27 K. Stöwe, *Solid State Sci.*, 2003, **5**, 765–769.

28 (a) J. S. Smart, *Effective Field Theories of Magnetism*; Saunders, Philadelphia, PA, 1966. (b) C. Kittel, *Introduction to Solid State Physics*, 7th ed.; John Wiley and Sons: Hoboken, NJ, 1996.

29 X. B. Chen, S. H. Shen, L. J. Guo and S. S. Mao, *Chem. Rev.*, 2010, **110**, 6503−6570.

30 Z. J. Ma, Z. G. Yi, J. Sun and K. C. Wu, *J. Phys. Chem. C*, 2012, **116**, 25074−25080.

Graphical Abstract

A new mixed-chalcogenide $Dy_4S_4Te_3$ was synthesized by a facile high-temperature solid-state reaction based on energy gap engineering, whose polycrystalline powder shows photocatalytic-active to decompose organic pollutant Rhodamine B under halogen lamp irradiation. It opens a novel type of chalcogenide-based photocatalyst.

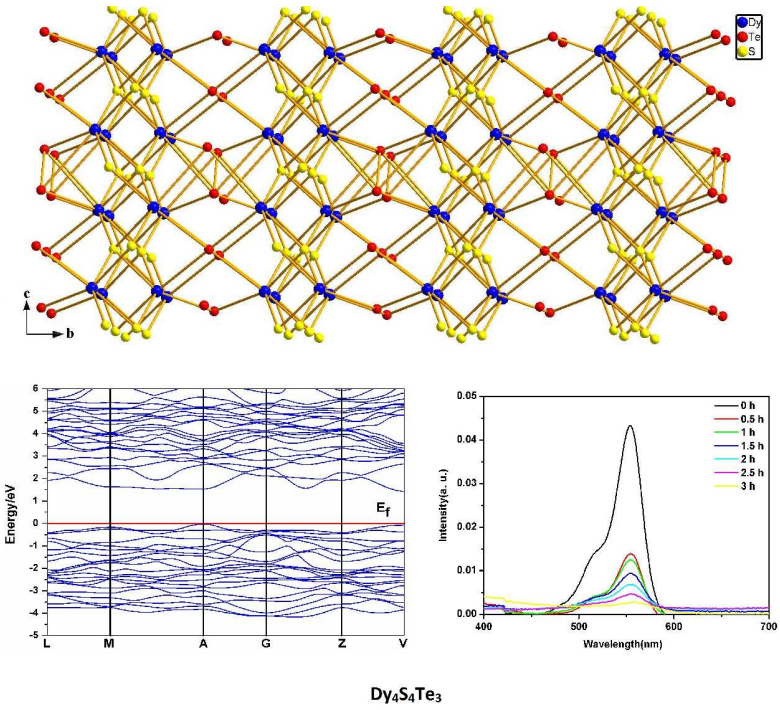

$Dy_4S_4Te_3$